Seasonal and diurnal variations of cloud systems over the East Tibetan Plateau and the East China: A Cloud-Resolving model study

Jinghua Chen[+, *], Xiaoqing Wu[#], Chunsong Lu[+] and Yan Yin[+]

[+]Collaborative Innovation Center on Forecast and Evaluation of Meteorological Disasters, Nanjing University of Information Science & Technology, Nanjing, China

[*]Key Laboratory of Meteorology and Ecological Environment of Hebei Province, Shijiazhuang, China

[#]Department of Geological and Atmospheric Sciences, Iowa State University, Ames, Iowa, USA

Submitted to. *J. Geophys. Res.: Atmos*

Corresponding author, Dr. Jinghua Chen, School of Atmospheric Physics, Nanjing University of Information Science & Technology, Nanjing, China. E-mail: jhchen@nuist.edu.cn

Abstract

Seasonal and diurnal variations of the cloud are profoundly affected by the large-scale environment and the local topography. In this study, the one-year-long simulation was conducted by a two-dimensional Cloud Resolving Model over the eastern Tibetan Plateau (ETP) and two sub-region of East China (EC), which are the middle and low reaches of the Yangtze River and Pearl River Delta. It found that deep convections (DCCs) can hardly happen in the cold season over the ETP while it can happen all the year around over the EC, and it is about 20-30% thinner in the ETP than in the EC. Most of EC rainfall events (Precipitation Intensity, PI> 2.5 mm hr^{-1}) relates to DCCs with cloud ice processes during the warm season. Because of the high elevation, the ETP warm-season freezing level is much lower than that of EC, making a favorable condition for cloud ice processes. DCCs are responsible for the diurnal variations of warm-season rainfall in all the regions. Warn-season DCCs have the greatest total cloud water content and frequency in the afternoon over the ETP, resulting in the afternoon peak of rainfall events. Besides the afternoon peak, rainfall events also have a nocturnal peak due to the DCCs over the ETP in spring, summer, and autumn. Strong surface heat fluxes around noon can trigger or promote DCCs in spring, summer, and autumn over the ETP, but only produce cumulus in winter due to the cold and dry environment.

1. Introduction

The Tibetan Plateau (TP) is discovered as an important heat source in boreal summer and heat sink in winter due to its towering and expansive topography [Luo and Yanai 1984; Ge et al., 2019, Wang et al., 2019, Wu et al. 2012; Zhao and Chen 2001]. During the warm season, the TP acts as a great heating source in the middle troposphere and provides an effective driving force for the upward motion, which could be a complementary forcing for the cloud development and even act as a critical player the deep convection under particular conditions over the TP [Chen et al. 2017b; Luo and Yanai 1983, 1984; Fu et al. 2020]. On the other hand, the grand surface of the TP is a great heat sink during winter [Yanai and Tomita 1998; Wu et al. 2019], which will make the atmosphere stable and impose a negative effect on the cloud development. The particular terrain of the TP as well as the large-scale circulation will lead to distinguished seasonal variations in cloud systems. Previous studies have suggested that the precipiatation over the TP, espically for the heavy rainfall, shows solid relationship to the moisture transported from the south. This process closely related to circulation and moisture condition over the India peninsula, which depens on the India Summer Monsoon (ISM) activities. Similarly, affected by the East Asia Monsoon (EAM), East China shows remarkable seasonal variations in cloud features (e.g., cloud cover, cloud water, precipitation) [Huang and Chan 2012]. During the warm season, there are amount of water vapor transported from the ocean by the monsoon circulation, resulting in more frequency of high cloud water content and plenty precipitation. Therefore, drastic seasonal variations in the cloud systems are expected over the East China because of the activities of the monsoon circulation [Chen et al. 2011; Ding 1992].

Cloud, which includes plenty of hydrometeor particles and water vapor, is important player in the earth-atmosphere energy balance through absorbing or reflecting the radiation. Cloud also acts as a key role in the water cycle and modifies the energy budget through releasing/consuming heat in water phase transition processes in cloud generation and precipitation processes [Dai 2001; Dai et al. 1999]. The macroscopic climatological properties (e. g., cloud cover, cloud water path) of cloud over the East China have been widely studied [Dai et al. 2007; Zhou et al. 2008]. Because precipitation over most of China occurs mainly from June to August [Tao and Chen 1987; Ding 1992] and the diurnal cycle is strongest during the summer [Dai et al. 2007], most previous studies focus on the characteristics of precipitation in the warm season [Zhou et al. 2008]. It has been reported that the diurnal harmonic dominates daily variations of precipitation over most of eastern China. For example, a late-afternoon maximum over southeastern and northeastern China, and a near-midnight maximum over the eastern periphery of the Tibetan Plateau are seen in rain gauge measurements [Zhou et al. 2008]. Nocturnal precipitation is also reported by previous studies [e.g., Chen et al. 2018; Singh and Nakamura 2009]. The cloud and precipitation closely link to the large-scale circulation and local environment (e.g., land use, terrain) and their characteristics will differ from place to place [Chen et al. 2017a; Dai 2001; Dai et al. 2007]. The particular effects of the TP's topography (e.g, surface heating, terrain blocking) profoundly affect the seasonal variations and diurnal structure of cloud system and precipitation [Fujinami et al. 2005; Xu and Zipser 2010]. However, the detailed and systematic seasonal characteristics of the cloud system over the TP are still need to be further investigated, e.g., the cloud properties that caused the diurnal cycle of precipitation in different seasons.

The objectives of the study are to simulate seasonal and diurnal variations of clouds and precipitation over two distinct regions (ETP and EC) using the cloud-resolving model, and to understand the impacts of large-scale circulation, topography and physical processes on the precipitation and cloud characteristics. The paper is organized as follows. Section 2 describes the datasets and model configuration. Seasonal and diurnal variations of precipitation and clouds are discussed in Section 3 and Section 4, respectively. Summary and discussion are given in Section 5.

2. Data and Model

a. Model descriptions

Usually, the cloud-scale simulation of year-long period could consume plenty of calculation and storage resource, and it is expansive to complete such experiments. In this study, a two-dimensional cloud-resolving model (CRM) is employed to conduct the year-long cloud-scale simulation. This model is an anelastic cloud model version originally developed by Clark et al. [1996] and was imposed with large-scale forcing and the modifications to physical processes for the long-term simulations of cloud systems [e.g., Grabowski et al. 1996; Wu et al. 1998; Wu et al. 2007; Wu et al. 1999]. The Kessler-type bulk warm rain parameterization [Kessler 1969] and the Koenig-Murray bulk ice parameterization [Koenig and Murray 1976] are involved in the model. Two classes of ice, referred to as ice A and ice B, are considered by the model, for which both the mixing ratio and the number concentration equations are solved. Ice A field (typically associated with unrimed or lightly rimed ice particles) is formed by either heterogeneous nucleation of pristine ice crystals, and ice B is usually associated with heavily rimed particles (e.g., graupel) of fast-falling speed and high-density, which originates from the interaction of the

rain field with the ice A. The surface heat fluxes in the model is calculated by the parameterization based on the study of Liu et al. [1979]. However, this parameterization is developed for the tropical ocean regions is not suitable over the land. For simplification, the surface heat fluxes are prescribed by the ERA-Interim surface heat fluxes dataset in the model. More detailed information about this model can refer to the cited literatures [e.g., Clark et al. 1996; Chen et al. 2017b].

b. Data and experimental designs

The model is forced by the large-scale advection terms, which mimics the effects of the large-scale flow on the temperature and moisture fields [e.g., Yanai et al. 1973]. Here, the large-scale horizontal and vertical advection of temperature and moisture is computed from the ERA-Interim reanalysis (hereafter ERAINT) [Dee et al. 2011]. According to the study of Yanai and Tomita [1998], the calculation results are sensitive to the p-velocity. Therefore, the p-velocity is recalculated from the horizontal divergence by vertically integrating the continuity equations. The detailed descriptions of the calculation processes are referred to Yanai and Tomita [1998] and Chen et al. [2015].

Based on the previous studies [Chen et al. 2017, 2019], the model performance shows great dependency on the reliability of the input data and varies in different regions. Therefore, the eastern Tibetan Plateau (ETP) is selected to investigate the cloud seasonal variations over the TP. The weather and climate of East China are profoundly affected by the EAM [Ding 1992]. According to the invading processes and route of EAM, the Pearl River Delta (PRD) and the Middle and Lower reaches of Yangtze River (MLYR) are influenced by the EAM in different

degrees. Usually, the PRD is firstly affected by the monsoon circulation in early May and the effects of EAM fade away in September [Ding and Chan, 2005]. The MLYR is a flatland in East China and is famous in the meteorology field for the Meiyu period during the early summer, which also is a distinct seasonal characteristics for this region. These three regions are shown in Fig. 1 and they experience different circulation patterns and moisture conditions, which will lead to distinguishing cloud and precipitation Then, one-year simulation (2010) is conducted for each region to examine the physical processes responsible for the cloud variations.

3. Seasonal variations of precipitation and clouds

Figure 2 shows the year-long daily precipitation from simulations, TRMM observations and ERAINT reanalysis system. The model can capture the seasonal variations of the precipitation for PRD, MLYR and ETP, and shows a better performance over the MLYR, which has a highest correlation coefficient (0.44) with the TRMM dataset among all the regions. Comparing to TRMM dataset, the model underestimated the heavy rainfall events over these three regions (e.g., 21/May of PRD, 17/Dec of MLYR and 21/May of ETP in Fig. 2). The large-scale forcing used to drive the model is computed from the ERAINT reanalysis dataset. Therefore, the simulated precipitation displays a similar evolutions with the ERAINT (Fig. 2). On the other hand, the uncertainties of the reanalysis dataset can be brought into the model results. For example, when the reanalysis lost its reliability (e.g., the rainfall event around 8/Oct. of PRD), the model does not reproduce the precipitation like the observation. The ETP experiences a dryer climate than that of MLYR and PRD (Fig. 2), and its precipitation mostly concentrated in the period from May to August. While heavy rainfall events (> 10 mm d^{-1}) occurres during the cold season (e.g., December) in the flatland (e.g., PRD and MLYR).

Comparing with MLYR and PRD, the model and the ERAINT show wet biases over the ETP as well as the ERAINT (Fig. 2c). According the study of Gao and Liu [2013], the TRMM precipitation generally tends to overestimate light rainfall (0-10 mm d^{-1}) and underestimate moderate and heavy rainfall (>10mm d^{-1}). These features would bring some uncertainties to the assessment of the rainfall amount. Overall, the model captures the features of the seasonal rainfall evolutions over these three regions with some biases in the simulated rainfall amount (Fig. 2).

Figure 3 presents the monthly averaged profiles of total cloud water content (TCWC) and the temperature for three regions. Evolutions of temperature and clouds for MLYR and PRD represent typical seasonal variations of a summer monsoon climate. The temperature reaches the maximum over two regions reach their maximum temperature in summer (June, July and August, or JJA) and the highest monthly temperature near the surface is over 25 °C (Figs. 3b and d). Meanwhile, the level of the maximum TCWC in PRD is increasing in April (Fig. 3a) when PRD experiences a pre-rainy season. The temperature near the surface in the ETP is much lower than in the lowland (e.g., PRD and MLYR), which is a consequence of its extreme high elevation. When the warm season arrives, the clouds become active over the ETP (Fig. 3e). However, the ETP clouds do not develop as high as the flatland clouds (Fig. 3a, c and e). Meanwhile, it is noticed that the monthly domain-averaged near-surface temperature is below 10 °C even in the warmest month (July in Fig. 3f) over ETP, and the temperature drops to 0 °C below 1 km above the ground level (AGL). This feature would induce to cloud ice processes occurring below 1 km AGL in the warm season over ETP, which is much lower than that of the lowland (over 4 km AGL).

178

179 The MLYR summer rainfall is profoundly affected by the EAM (Ding and Chan 2005).
180 However, the TCWC in the cold season is not much smaller thant the warm season TCWC in
181 the MLYR as shown in Fig. 3c. Here, the monthly cloud liquid water content (LWC) and ice
182 water content (IWC) are examined in Fig. 4. It shows that the level of the maximum LWC
183 increased in May and there is a thin cloud layer appearing few hundred meters above the surface
184 in MLYR (Fig. 4c). The maximum monthly IWC appears in the last month of winter (February)
185 in MLYR (Fig. 4d). The altitude of maximum IWC increase as the weather gets warmer (Fig. 4d)
186 in MLYR. The level of maximum LWC in PRD can be as high as 4 km AGL in winter (Fig. 4a),
187 which corresponds a 0 °C level at round 4 km AGL (Fig. 3b). However, the altitude of the
188 maximum IWC in PRD increases in the warm season and is as high as 10 km AGL in June. This
189 reflects that deep cloud systems can develop higher in the warm season [Chen et al. 2017). Over
190 the ETP, the level of the maximum LWC is below 1 km AGL because of the low temperature
191 (Fig. 3f), and the maximum IWC occurres at the level around 4 km in June (Fig. 4f), which is
192 much lower than the flatland (8 km AGL in MLYR and 10 km AGL in PRD, Figs. 3b and d).
193 Also, it is noticed that there are two layers of LWC in ETP, the lower one has greater LWC than
194 the upper layer. Observational results show that the cumulus cloud is an important type of cloud
195 and is frequent in the warm season over the TP [Li and Zhang 2017; Li et al. 2004]. The low
196 layer of high concentration LWC over ETP is mostly caused by the cumulus cloud.
197

198 The top and base altitudes of all cloud cells for different regions are shown in Fig. 5. The
199 frequency of each cloud cell is defined as the ratio of the cloud cell grids to the total grid number
200 in the region. The deep cloud usually has characteristics of lower cloud base and higher cloud

top. When the deep cloud occurres frequently, there will be a left-plume shape in each panel of Fig. 5. This feature is obtained in spring, summer and autumn of the MLYR (Figs. 5e-g), and in spring and summer of ETP (Figs. 5i and j), suggesting that the deep cloud (e.g., deep convections) is prevailing during these seasons in these regions. When it comes to PRD, the left-plume structure is not shown in the Figs.5a-d, indicating that the deep cloud with lower cloud base and higher cloud top is not dominated type of cloud. Meanwhile, the cloud top of deep cloud is over 10 km AGL in MLYR and it is below 8 km AGL in ETP. The depth of the deepest cloud (mostly the deep convection) is over 10 km in MLYR, and has no dramatically seasonal variation from spring to autumn (Figs. 5e-g). The depth of ETP deep cloud is about 20-30% thinner than that of MLYR, and has an increasing tendency of about 10% from spring to summer. This suggests that the cloud can develop higher and becomes more vigorous in the warm season because of the favorable large-scale circulation and the enhanced surface heat fluxes, which agrees with the results of the sensitive study [Chen et al. 2019]. It is noticed that there is a left-plume structure below 6 km AGL in Fig. 5k, which is not a typical cloud top altitude and depth for a deep convection. When the winter comes, the development of clouds over ETP is substantially restricted (Fig. 5f), which is largely due to the reduced moisture and surface heating along with the retreat of the Indian summer monsoon.

Benefiting to the humid and warm environment, clouds in PRD are more active and can develop to higher level throughout the year than those in other regions. For example, the cloud with a depth more than 8 km can develop to 16 km AGL in PRD during summer (Fig. 5b). Meanwhile, there are seasonal variations in the deep cloud's top with a highest in summer and lowest in winter in PRD (Figs. 5a-d). Cloud top of deep cloud in MLYR does not show

224 significant seasonal variations, and the cloud top of deep cloud is 4 km lower than that in PRD.
225 The typical deep convection, which has a cloud base below 1 km AGL and a cloud top over 10
226 km AGL, can occur throughout the year in the MLYR (Figs. 5e-h). Moreover, other type of deep
227 clouds, which has a cloud base around 2 km AGL and a depth of 6-8 km, can develop in MLYR
228 during spring, autumn, and winter. These clouds with deep depth mostly have great precipitation
229 capacities, which are mostly the deep stratiform clouds generated during synoptic processes (e.g.,
230 frontal systems). When it comes to ETP, it is shown that the deep cloud's top (cloud depth > 5
231 km) shrinks dramatically to a level below 8 km AGL (Figs. 5i-k). Cloud depth shows seasonal
232 variations with the thinnest cloud in winter and the deepest cloud in ETP during summer, which
233 larhely relates to the its local theremal heating and moisture supply due to the large-scale
234 circulation. Comparing with the clouds of the lowland (e.g., the MLYR and PRD), the cloud
235 depth in ETP is much thinner, which is only 60-70% of the deepest cloud in the lowland for the
236 same season (e.g., Fig. 5). These results agree with the satellite observations [Qie et al. 2014].
237 The deep cloud systems can hardly develop in ETP during winter because of the dry and cold
238 environment, and all the cloud cells' developments are restricted. It is noticed that there is a
239 maximum frequency at the lower-left corner of the Figs. 5i-l, which largely reflects the high
240 frequency of cumulus clouds with small cloud depth in ETP throughout the year.
241
242 **4. Diurnal variations of precipitation and clouds**
243 Diurnal cycles of precipitation and cloud are important factors for local weather and
244 climate [Zhou et al. 2008]. The model output provides an opportunity to examine the
245 precipitation and cloud's diurnal variations concurrently. Here, the precipitation intensity (PI)
246 represents the domain-averaged result for each region, and rainfall events are classified into five

types as shown in Table 1. These five types (I-V) are defined as little, small, middle, strong, and heavy rain events, respectively. As a result, the precipitation capacity of the precipitating cloud for each rainfall type becomes more and more greater from type I to type V. Based on this classification, frequencies of all these five-type rainfall events for all the three regions are obtained using the 15-minutes interval model output, which are shown in Fig. 6. The frequency of type V varies with seasons and regions. The heavy rainfall events in PRD can account almost 15% of the total precipitation events in summer and it is less than 3% in winter, which corresponds with the deep cloud's seasonal variations as shown in Fig. 5. The frequency of the rainfall events with a PI below 2.5 mm hr^{-1} do not show dramatically seasonal differences in PRD (Fig. 6a-d), indicating that these clouds except the deep cloud appear in similar frequency. For MLYR, each type rainfall event has seasonal variations in frequency. Heavy rainfall event reaches its most stirring period in the warm season in MLYR. The frequency of heavy rainfall over MLYR is about 10% in summer, which is smaller than that of PRD (Figs. 6b and f). Dramatically seasonal variations are obtained in ETP (Figs. 6i-k). Type V rainfall, which is largely produced by deep convections over ETP, is most frequent in summer, followed by spring and autumn. The strongest rainfall events can hardly happen in winter. These results agree with the frequency of deep cloud shown in Figs. 5i-l.

Frequency of heavy rainfall shows diurnal variations with a noon peak in spring and a later-after peak in summer over PRD (Figs. 6a and b). These results suggest that the rainfall events with greatest PI (type V) mostly happen in noon (later-afternoon) in spring (summer) over PRD, which agrees with the observational results [Zhou et al. 2008]. However, other types of precipitation do not show significant diurnal variation signals in spring and autumn. In winter,

frequency of each type of rainfall event do not show dramatically diurnal variations in PRD (Fig. 6d). Comparing with spring and winter, summer and autumn are the seasons with diurnal cycle variations of precipitation in MLYR (Figs. 6e-h). The little rain events' frequency in the warm season shows doublet diurnal cycle structure with one peak in early morning and another one in later night in MLYR (Fig. 6f). Doublet structure in warm-season precipitation's diurnal cycle is also discovered in the Middle Yangtze River Valley using the ground-based observational datasets [Zhou et al. 2008]. While the other types of rainfall events in the warm season show peak frequencies around noon in MLYR, and the PI is greater; the singlet structure is more obvious (Fig. 6f). Zhou et al. [2008] suggested that the precipitation, which is estimated using Artificial Neural Networks and Tropical Rainfall Measuring Mission 3B42, missed the early morning peak in the diurnal cycle of precipitation frequency in MLYR. The early morning frequency peak is mostly contributed by the little rain events (Fig. 6f), which implies that the dataset will underestimate the frequency of little rain events in MLYR. The diurnal cycle signals of types II-V precipitation become weak in autumn and disappear in winter in MLYR (Figs. 6g-h). Meanwhile, frequencies of strong and heavy rainfall events in MLYR become small in autumn and winter. However, frequency of small rainfall events hit its maximum values in winter with no diurnal variations. Affected by the EASM, both MLYR and PRD reach their rainiest season in summer, and the rainfall events with a PI greater than 2.5 mm hr^{-1} have peaks at noon in MLYR and afternoon in PRD. According the study of [Xu and Zipser 2011], the deep convection has a peak around noon in MLYR and later-afternoon in PRD. This suggests that deep convections make important contributions to the peak frequency of the warm-season strong and heavy rainfall events at around noon (afternoon) in MLYR (PRD).

293 Comparing to the lowland, frequencies of all the rainfall types except small rainfall in
294 ETP show more remarkable diurnal variations in spring, summer and autumn (Figs. 6i-k). The
295 frequency of small rainfall events shows no remarkable signal in diurnal variations in spring,
296 summer and autumn. Here, types III-V rainfall events are considered as the great rainfall events
297 in ETP. The great rainfall events can hardly occur in winter (Fig. 6l), leading to rainless winter as
298 denoted in the TRMM dataset (Fig. 2c). Great rainfall events over ETP activate in spring with a
299 frequency peak around noon (Fig. 5i). When summer comes, the great rainfall events become
300 more active (Fig. 6j) and show doublet structure in the frequency's diurnal variation. The main
301 peak is at afternoon, which can be over 20% of the total rainfall events. Another peak around
302 early morning is much weak, which is less than 10% of the total rainfall events. Using the
303 TRMM datasets, Fu et al. [2006] found that there is a strongest diurnal cycle of precipitation
304 occurring over the central TP with a peak at later afternoon and a low at about 05:00 LST. These
305 results confirm the diurnal cycle structure in Fig. 6j, and indirectly indicate that most rain events
306 are convective in the Plateau summer [Fu et al. 2006].
307
308 Deep convection is a type cloud with great precipitation capacity. Here, deep convective
309 clouds are separared out by the criterion that the cloud depth is greater than 10 km over the
310 lowland (5.5 km over ETP), and the cloud top is greater than 12 km AGL over the lowland (6 km
311 AGL over ETP). This definition considers the differences in cloud depth between the TP and the
312 lowland (e.g., Fig. 5). The basic idea behind this definition is that, deep convection normally
313 extends vertically through most of the troposphere, and the atmosphere column is much thinner
314 in ETP than in the lowland. Comparing to the uniform definition over all the regions, this
315 definition allows more deep convection samples over the TP. Figures 7 and 8 show the diurnal

316 cycle of averaged deep convection profiles of the frequency (Fig.7) and the TCWC (Fig. 8),
317 respectively, for each season over PRD, MLYR, and ETP. The TCWC can be used to measure
318 the precipitation capacity and intensity of deep convections, which is be helpful to understand
319 the precipitation diurnal variations as shown in Fig. 6. The averaged profiles of deep
320 convection's TCWC and frequency show corresponding seasonal variations to the great rainfall
321 events (Figs. 6, 7and 8). Both the PRD and MLYR have deep convections with great TCWC and
322 frequency in summer (Figs. 7b, f and 8b, f), which agrees with the great rainfall events' seasonal
323 variations as shown Figs. 6b and f. It is notced that the MLYR deep convections shows a peak of
324 frequency in winter. However, the mean MLYR TCWC suggests that these deep convections in
325 winter have the smaller TCWC than in summer. The PRD deep convections show a maximum
326 frequency and TCWC around noon in summer (Figs. 7b and 8b). However, great rainfall events
327 (PI >2.5 mm hr^{-1}) show great frequency in afternoon (Fig. 6b), implying that other deep cloud
328 systems make contributions to the afternoon great rainfall events. The TCWC of the summer
329 deep convection reaches its maximum value at around 8 km AGL and around noon in the
330 MLYR, and it can be 10 km AGL during noon to later afternoon in PRD (Figs. 8b and f).
331 However, it is reported that the MLYR rainfall of midsummer has a peak in later afternoon
332 (around 16:00 LST) [Chen et al. 2009]. Figure 7f indicates that there are high frequency deep
333 convections in later afternoon, suggesting that the later afternoon peak of the MLYR rainfall
334 [Chen et al. 2009] relates to these high frequency deep convections. The PRD convections show
335 a higher maximum TCWC level than that of MLYR in all the seasons (Figs. 8a-h), suggesting
336 that convections are more exuberant in PRD than that in MLYR. The TCWC of convections
337 over the lowland (e.g., the PRD and the MLYR) shows the diurnal cycle in spring, summer, and
338 autumn, and there is no significant diurnal cycle signal for the TCWC in winter over the lowland

(Figs. 8d and h). However, the frequency of the deep convections over these regions has diurnal variations in cold season over these regions (Figs. 7d and h), which could leads to a diurnal cycle in precipitation in cold season as reported by Huang and Chan [2012].

Figures 5 and 6 show that the ETP has the most remarkable seasonal variations and the most dramatically diurnal cycle in precipitation. These features also appear in the TCWC and frequency of deep convections (Figs. 7i-l and 8i-l). Deep convection gets the most favorable conditions for its triggering and development in summer, followed by spring and autumn (Figs. 7i-k and 8i-k). Previous studies reported that deep convections activities and precipitation over the ETP have an afternoon peak because of the influence of the surface heat flux in the warm season [e.g., Chen et al. 2018; Chen et al. 2017a; Li 2018). Figure 9 shows that there are remarkble diurnal variations with a peak at around noon in the surface heat fluxes (including sensible heat flux and latent heat flux) over the ETP in each seasons. Figures 7j and 8j show that there are frequencnt deep convections with high TCWC at afternoon over the ETP, which will make great contribution to the early-afternoon precipitation peak (Fig. 6j). Warm-season nocturnal rainfall over the ETP has been reported by Chen et al. [2018]. The frequency of the deep convections shows a second frequency period at night in the warm season (Fig. 7j). However, deep convections at night has smaller TCWC than the afternoon deep convections (Fig. 8j), which implies that the intensity of the nocturnal rainfall events is relative weak. The warm-season doublet structure in the deep convections' diurnal frequency and the TCWC (Figs. 7j and 8j) corresponds to the diurnal structure of the rainfall events greater than 2.5 mm hr^{-1} (Fig. 6j). According to the TRMM observations [Singh and Nakamura 2009], precipitation of the central TP shows a second peak at midnight in the warm season, which is similar to the diurnal

structures of TCWC and the frequency of the deep convection over the ETP (Figs. 7j and 8j). This suggests that deep convections not only take the main responsibility for the afternoon peak of precipitation but also make a great contribution to the nocturnal precipitation peak. Doublet structure in deep convection frequency is also obtained in spring and autumn (Figs. 7i and k) and the maximum frequency in autumn appears during the night (Fig. 7k). However, nocturnal deep convections are small in the TCWC (Figs. 8i and k), which will possibly lead to weak-intensity rainfall events. Winter is an unamiable season for the trigger and development of deep convections (Figs. 7l and 8l) in the ETP, which is mostly due to the dry and cold conditions.

Beside deep convections, cumulus cloud (Cu) plays an important role in the earth-atmosphere energy budget, and is one of the dominant cloud types over the TP [Li and Zhang 2017]. Cu could transport heat and moisture near the surface to the free atmosphere [Wang and Zhang 2014], causing ventilation of the planet boundary layer. Meanwhile, convections over the TP can evolve from dry and shallow convection in the morning to wet and deep convection in the afternoon [Yang et al. 2004]. Here, Cu is defined as a cloud cell with a depth smaller than 1.5 km and cloud top height below 6.5 km AGL, which can exclude high-level thin cloud (e.g., cirrus). Figure 10 shows the diurnal cycle for the averaged TCWC of the shallow clouds with different cloud bases. For PRD, Cu is active throughout the year and there is no significant signal in the TCWC diurnal cycle for each season (Figs. 10a-d). The diurnal cycle of Cu's frequency shows a double layers of maximum frequency in spring (Fig. 11a) over PRD, one is around 2 km AGL and another is around 3.5 km AGL. The other seasons show maximum frequencies at around 2 km (Figs. 11b-d). Comparing to the PRD, the MLYR Cu is lower in the TCWC (Figs. 10e-h) and has diurnal variations in the TCWC and frequency (Figs. 10e-h and 11e-h). The most

frequent season for the MLYR Cu is winter while Cu has the greater TCWC in summer (Figs. 10f and h). The cloud base of the Cu with the maximum TCWC in MLYR increases after 07:00 LST in spring, summer and autumn (Figs. 10e-g). The period with the most frequency period of Cu is at night in spring, summer and autumn, and it becomes around noon in winter in the MLYR. Moreover, the cloud base of the most frequency Cu in winter is about 2 km AGL (Fig. 11h) over the MLYR, which is higher than in other seasons (Figs. 11e-h). Figures 7e-h show that the deep convection has an antiphase in the diurnal frequency variation with the frequency of Cu (Figs. 11e-h), implying that the maximum time of Cu frequency corresponds to a small frequency of deep convection, and vice versa. Moisture and energy will be transported to the MLYR by the monsoon circulation during the warm season [Ding and Chan 2005), which can make a favorable environment for the trigger and development of deep convection. Moreover, the warm-season precipitation and deep convection prefer to occur during noon to afternoon [Li et al. 2018] (e.g., Figs. 7 and 8), which implies that the thermal convection is vigorous and can develop to deep convection. When the monsoon fades out in winter, the atmosphere becomes dry and deep clouds cannot be triggered frequently in the MLYR, leading to more opportunity to generate Cu.

Cu over the ETP shows clearly seasonal variations in the TCWC with the maximum value in summer, followed by autumn, spring and winter (Figs. 10i-l). These seasonal variations reflect the moisture and thermal conditions associated with the India Monsoon circulation. The cloud base of Cu with the maximum TCWC increases after 09:00 LST and reaches its maximum value at around noon in the ETP (Figs. 10i-l), which is mostly affected by the surface sensible heat fluxes (Fig. 9). Cu's maximum frequency period is around 07:00~08:00 LST in spring,

summer and autumn, and it is around 14:00 LST in winter (Figs. 11i-l). Moreover, Cu's frequency is increasing after 18:00 LST in spring, summer and autumn in the ETP. Panels i-k in Figs 6, 7 and 8 show that most deep convections with great TCWC develop during the noon to afternoon and leads to great rainfall events. The precipitation process will consume the moisture of the deep convections and terminate deep convections. When the rainfall events associated with deep convections are over, shallow clouds remain and contribute to the increasing of the Cu's frequency after 18:00 LST. The maximum frequency of Cu occurs at round 13:00 LST in winter over the ETP (Fig. 11l)., which corresponds to the period of strong surface heat fluxes (Fig. 9l). While the maximum frequency and TCWC of deep convection in other seasons is around 13:00 LST (Figs. 7i-k and 8i-k) in the ETP. According to the sensitivity study [Chen et al. 2019], the surface heat flux is an important player in the triggering and development of warm-season deep convections and the heavy rainfall events. When winter is coming over the ETP, the atmosphere becomes cold and dry, which is a tough environment for deep cloud's development, especially for the deep convections. Under this background, the strong surface heating around noon (Fig. 9l) can hardly trigger deep convections but trigger cumulus in winter (Fig. 11l) in the ETP. Moreover, Cu around noon has much smaller TCWC in winter that in the other seasons (Figs. 10i-k). This suggests g that Cu can be triggered by the surface heating effects around noon, and its TCWC is low due to the cold and dry environment in winter. However, the enhanced surface heat fluxes (Fig. 9b) is helpful to trigger deep convections in the warm and humid atmosphere of the warm season (Figs. 7j and 8j).

5. Conclusion and discussion

Seasonal and diurnal variations of cloud and precipitation are investigated by the 2D Cloud-Resolving Model over the monsoon areas (East China) and the Eastern Tibetan Plateau. Differences in clouds between the monsoon areas and ETP in seasonal and diurnal variations are discussed. The highlighted conclusions are summarized as follow.

Affected by the monsoon system, most of the precipitation happens in the warm season over the monsoon regions. In PRD, the maximum values of the TCWC and its level are getting higher and higher from April to June. This suggests that the cloud systems become deeper and the cloud ice process is active, which will lead to great rainfall events in the warm season in PRD. Deep cloud systems with ices become active and powerful in May, and reaches their maximum period in July, resulting in an increasing tendency in the peak level of IWC from May to July. This feature implicates that the great rainfall events due to deep cloud systems in the warm season are closely related to the cloud ice processes, which requires that the deep cloud extends to a higher level (>8 km AGL) in PRD. Most of cloud activities over ETP happen during May to October and most of the precipitation concentrates in the same period. Because of the low surface temperature due to the high elevation, clouds over ETP can reach the zero temperature level at a low altitude in the warm season, which can be smaller than 1 km AGL. This demonstrates that the cloud ice processes can happen in most clouds during the warm season.

Deep convections are prevailing in spring, summer and autumn over MLYR and have the greatest TCWC in summer, which make important contributions to the warm-season rainfall amount. Comparing to MLYR, deep convections can extend to a higher level but constitute a lower percentage of the total cloud cells over PRD. However, other deep clouds are frequent in the warm season and can develop to the level over 10 km AGL, which could make contributions

453 to the rainfall in PRD. Affected by the thin atmospheric column, most clouds are restricted below
454 10 km AGL over ETP. Because of the favorable large-scale circulation and strong heating effects
455 due to surface heat fluxes, deep convections are most popular and have the greatest TCWC in
456 summer over ETP. However, deep convections in ETP are 20-30% thinner than in the lowland
457 (e.g., the MLYR and PRD), and can hardly happen in winter.
458
459 The heavy rainfall event (PI> 5 mm hr^{-1}) in PRD shows a diurnal cycle with a afternoon
460 peak in spring and summer, corresponding to the diurnal variations of the deep cloud with
461 greatest precipitation capacity. While other rainfall events do not show significant diurnal
462 variations throughout the year in PRD. Frequency of great rainfall events (PI>2.5 mm hr^{-1}) in
463 MLYR shows diurnal variations with a afternoon peak in the warm season. Moreover, deep
464 convections in MLYR can develop higher in summer, which could make great contribution to
465 the summer rainfall. Deep convections during summer have the greatest TCWC and frequency in
466 afternoon over ETP, resulting in the large frequency of the rainfall events (PI> 2.5 mm hr^{-1})
467 during this period. Beside the afternoon peak, the great rainfall events (PI> 2.5 mm hr^{-1}) also
468 have another frequency period during night in ETP, which agrees the observational results (Chen
469 et al., 2018). Deep convections also show second nocturnal peaks in frequency and the TCWC
470 over ETP, which is responsibility for the high frequency of the nocturnal great rainfall events.
471
472 Cumulus cloud does not show significant diurnal variations in all the seasons in PRD.
473 However, diurnal variations of Cu are obtained in MLYR and ETP. Usually, the cloud base of
474 Cu with the maximum TCWC is increasing from 09:00 LST to 13:00 LST over these two regions
475 in spring, summer and autumn. However, the maximum frequency of Cu is at night during

spring, summer and autumn in MLYR and ETP. During the cold season, Cu reaches its maximums frequency and TCWC around noon in ETP, which is mostly caused by heating due to the surface heat fluxes. The strong surface heat fluxes around noon can promote the development of cloud or trigger deep convections under the suitable moisture and thermal conditions (e.g., the warm season) over ETP. However, the strong surface heat flux around noon can only trigger Cu due to the ETP's cold and dry atmosphere in the cold season.

The investigation and analysis of cloud systems in this study are mainly based on the simulations by the Cloud-Resolving Model. Although the model performance over several regions (e.g., the Great Plain of America, East China and the Tibetan Plateau) has been examined in previous studies [Chen et al. 2017a; Chen et al. 2017b; Grabowski et al. 1998; Wu et al. 1998], uncertainties can be brought in by the experimental design (e.g., the periodic boundary condition) and the large-scale forcing (e.g., uncertainty of the reanalysis dataset). Moreover, the mechanism for the triggering and development of nocturnal deep convections over the ETP needs to be further investigated by the well-designed numerical experiments.

Acknowledgements: The ERA-Interim reanalysis dataset can be accessed via website (https://www.ecmwf.int/node/8174), the TRMM precipitation products are available on the website https://pmm.nasa.gov/data-access/downloads/trmm, and the model output is in the account chenjh@157.0.78.3 and can be accessed by contacting Dr. Chen (jhchen@nuist.edu.cn). This study was supported under the National Key R&D Program of China (2017YFA0604001) and National Science Foundation of China (41705118, 41775136, 41775096, 41705120, 41575133), the Natural science fund for colleges and universities in Jiangsu Province

499 (17KJB170010), China Scholarship Council, the Natural Science Foundation of Jiangsu Province
500 (BK20170945), the Open Fund of Key Laboratory of Meteorology and Ecological Environment
501 of Hebei Province and the National Center of Meteorology, Abu Dhabi, UAE under the UAE
502 Research Program for Rain Enhancement Science.
503

504 **References**

505 Chen, G., W. Sha, and T. Iwasaki, 2009: Diurnal variation of precipitation over southeastern
506 China: Spatial distribution and its seasonality. *J. Geophys. Res.: Atmos*, 114. D13103.
507 Chen, H., J. Li, and R. Yu, 2018: Warm season nocturnal rainfall over the eastern periphery of
508 the Tibetan Plateau and its relationship with rainfall events in adjacent regions. *Int. J.*
509 *Climatol.*, 38, 4786-4801.
510 Chen, J., X. Wu, Y. Yin, and H. Xiao, 2015: Characteristics of Heat Sources and Clouds over
511 Eastern China and the Tibetan Plateau in Boreal Summer. *J. Climate*, 28, 7279-7296.
512 Chen, J., X. Wu, Y. Yin, Q. Huang, and H. Xiao, 2017a: Characteristics of Cloud Systems over
513 the Tibetan Plateau and East China during Boreal Summer. *J. Climate*, 30, 3117-3137.
514 Chen, J., X. Wu, Y. Yin, C. Lu, H. Xiao, Q. Huang, and L. Deng, 2019: Thermal Effects of the
515 Surface Heat Flux on Cloud Systems over the Tibetan Plateau in Boreal Summer. *J. Climate*,
516 32, 4699-4714.
517 Chen, T.-C., W.-R. Huang, and M.-C. Yen, 2011: Interannual Variation of the Late Spring–Early
518 Summer Monsoon Rainfall in the Northern Part of the South China Sea. *J. Climate*, 24, 4295-
519 4313.
520 Chen, Y., Y. Fu, T. Xian, and X. Pan, 2017b: Characteristics of cloud cluster over the steep
521 southern slopes of the Himalayas observed by CloudSat. *Int. J. Climatol*, 37,4043-4052.

522 Clark, T., W. Hall, and J. Coen, 1996: Source Code Documentation for the Clark-Hall Cloud-
523 Scale Model Code Version G3CH01. *NCAR Tech. Note NCAR/TN-426 STR*, 137pp.
524 Dai, A., 2001: Global precipitation and thunderstorm frequencies. Part II: Diurnal variations. *J.*
525 *Climate*, 14, 1112-1128.
526 Dai, A., K. E. Trenberth, and T. R. Karl, 1999: Effects of Clouds, Soil Moisture, Precipitation,
527 and Water Vapor on Diurnal Temperature Range. *J. Climate*, 12, 2451-2473.
528 Dai, A., X. Lin, and K.-L. Hsu, 2007: The frequency, intensity, and diurnal cycle of precipitation
529 in surface and satellite observations over low-and mid-latitudes. *Clim. Dyn.*, 29, 727-744.
530 Dee, D. P., and Coauthors, 2011: The ERA-Interim reanalysis: Configuration and performance
531 of the data assimilation system. *Quart. J. Roy. Meteor. Soc.*, 137, 553–597.
532 Ding, Y., 1992: Summer monsoon rainfalls in China. *J. Meteor. Soc. Japan*, 70, 373-396.
533 Ding Y., and J. C. L. Chan, 2005: The East Asian summer monsoon: an overview. *Meteorol.*
534 *Atmos. Phy.*, 89, 117-142.
535 Fu, Y., and Coauthors, 2006: Tower mast of precipitation over the central Tibetan Plateau
536 summer. *Geophys. Res. Lett*, 33, L05802.
537 Fu Yunfei, and Coauthors, 2020: Land surface processes and summer cloud-precipitation
538 characteristics in the Tibetan Plateau and their effects on downstream weather: a review and
539 perspective, *National Sci. Rev.*, nwz226.
540 Fujinami, H., S. Nomura, and T. Yasunari, 2005: Characteristics of diurnal variations in
541 convection and precipitation over the southern Tibetan Plateau during summer. *Sola*, 1, 49-52.
542 Gao, Y. C., and M. F. Liu, 2013: Evaluation of high-resolution satellite precipitation products
543 using rain gauge observations over the Tibetan Plateau. *Hydrol. Earth Syst. Sci.*, 17, 837-849.

Ge, J., Q. You, and Y. Zhang, 2019: Effect of Tibetan Plateau heating on summer extreme precipitation in eastern China. *Atmos. Res.*, 218, 364-371.

Grabowski, W. W., X. Wu, and M. W. Moncrieff, 1996: Cloud-Resolving Modeling of Tropical Cloud Systems during Phase III of GATE. Part I: Two-Dimensional Experiments. *J. Atmos.* Sci., 53, 3684-3709.

Grabowski, W. W., X. Wu, M. W. Moncrieff, and W. D. Hall, 1998: Cloud-Resolving Modeling of Cloud Systems during Phase III of GATE. Part II: Effects of Resolution and the Third Spatial Dimension. *J. Atmos. Sci.*, 55, 3264-3282.

Huang, W.-R., and J. C. L. Chan, 2012: Seasonal variation of diurnal and semidiurnal rainfall over Southeast China. *Clim. Dyn.*, 39, 1913-1927.

Kessler, E., 1969: On the distribution and continuity of water substance in atmospheric circulation. *Meteor. Monogr., No.32, Amer. Meteor. Soc.*

Koenig, L. R., and F. W. Murray, 1976: Ice-bearing cumulus cloud evolution: Numerical simulation and general comparison against observations. *J. Appl. Meteorol*., 15, 747-762.

Li, J., 2018: Hourly station-based precipitation characteristics over the Tibetan Plateau. *Int. J. Climatol.*, 38, 1560-1570.

Li, P., K. Furtado, T. Zhou, H. Chen, J. Li, Z. Guo, and C. Xiao, 2018: The diurnal cycle of East Asian summer monsoon precipitation simulated by the Met Office Unified Model at convection-permitting scales. *Clim. Dyn.*, doi: https://doi.org/10.1007/s00382-018-4368-z

Li, Y., and M. Zhang, 2017: The Role of Shallow Convection over the Tibetan Plateau. *J. Climate*, 30, 5791-5803.

Li, Y., R. Yu, Y. Xu, and X. Zhang, 2004: Spatial distribution and seasonal variation of Cloud over China based on ISCCP data and surface observations. *J. Meteor. Soc. Japan*, 82, 761-773.

567 Liu, W. T., K. B. Katsaros, and J. A. Businger, 1979: Bulk Parameterization of Air-Sea
568 Exchanges of Heat and Water Vapor Including the Molecular Constraints at the Interface. *J.*
569 *Atmos. Sci.*, 36, 1722-1735.
570 Luo, H., and M. Yanai, 1983: The Large-Scale Circulation and Heat Sources over the Tibetan
571 Plateau and Surrounding Areas during the Early Summer of 1979. Part I: Precipitation and
572 Kinematic Analyses. *Mon. Wea. Rev.*, 111, 922-944.
573 Luo, H., and M. Yanai, 1984: The Large-Scale Circulation and Heat Sources over the Tibetan
574 Plateau and Surrounding Areas during the Early Summer of 1979. Part II: Heat and Moisture
575 Budgets. *Mon. Wea. Rev.*, 112, 966-989.
576 Qie, X., X. Wu, T. Yuan, J. Bian, and D. Lu, 2014: Comprehensive Pattern of Deep Convective
577 Systems over the Tibetan Plateau–South Asian Monsoon Region Based on TRMM Data. *J.*
578 *Climate*, 27, 6612-6626.
579 Singh, P., and K. Nakamura, 2009: Diurnal variation in summer precipitation over the central
580 Tibetan Plateau. *J. Geophy. Res: Atmos*, 114, D20107.
581 Tao, S., and L. Chen, 1987: A review of recent research on the East Asian summer monsoon in
582 China. Monsoon Meteorology, C. P. Chang and T. N. Krishnamurti, Eds., Oxford University
583 Press, 60–92.
584 Wang, X., and M. Zhang, 2014: Vertical velocity in shallow convection for different plume
585 types. *J. Adv. Model. Earth Sy.*, 6, 478-489.
586 Wang, M., J. Wang, A. Duan, J. Yang, and Y. Liu, 2019: Quasi-biweekly impact of the
587 atmospheric heat source over the Tibetan Plateau on summer rainfall in Eastern China. *Clim.*
588 *Dyn.*, 53, 4489-4504.

589 Wu, G., A. Duan, and Y. Liu, 2019: Atmospheric Heating Source Over the Tibetan Plateau and
590 Its Regional Climate Impact. *Oxford Research Encyclopedia of Climate Science*.
591 DOI:10.1093/acrefore/9780190228620.013.588
592 Wu, G., Y. Liu, B. He, Q. Bao, A. Duan, and F.-F. Jin, 2012: Thermal controls on the Asian
593 summer monsoon. *Sci. Rep.*, 2, 1-7.
594 Wu, X., W. W. Grabowski, and M. W. Moncrieff, 1998: Long-Term Behavior of Cloud Systems
595 in TOGA COARE and Their Interactions with Radiative and Surface Processes. Part I: Two-
596 Dimensional Modeling Study. *J. Atmos. Sci.*, 55, 2693-2714.
597 Wu, X., W. D. Hall, W. W. Grabowski, M. W. Moncrieff, W. D. Collins, and J. T. Kiehl, 1999:
598 Long-Term Behavior of Cloud Systems in TOGA COARE and Their Interactions with
599 Radiative and Surface Processes. Part II: Effects of Ice Microphysics on Cloud–Radiation
600 Interaction. *J. Atmos. Sci.*, 56, 3177-3195.
601 Wu, X., X. Z. Liang, and S. Park, 2007: Cloud-resolving model simulations over the ARM SGP.
602 *Mon. Wea. Rev.*, 135, 2841-2853.
603 Xu, W., and E. J. Zipser, 2: Diurnal Variations of Precipitation, Deep Convection, and Lightning
604 over and East of the Eastern Tibetan Plateau. *J. Climate*, 24, 448-465.
605 Yanai, M., S. Esbensen, and J.-H. Chu, 1973: Determination of Bulk Properties of Tropical
606 Cloud Clusters from Large-Scale Heat and Moisture Budgets. *J. Atmos. Sci.*, 30, 611-627.
607 Yanai, M., and T. Tomita, 1998: Seasonal and Interannual Variability of Atmospheric Heat
608 Sources and Moisture Sinks as Determined from NCEP–NCAR Reanalysis. *J. Climate*, 11,
609 463-482.

Yang, K., T. Koike, H. Fujii, T. Tamura, X. Xu, L. Bian, and M. Zhou, 2004: The daytime evolution of the atmospheric boundary layer and convection over the Tibetan Plateau: observations and simulations. *J. Meteor. Soc. Japan*, 82, 1777-1792.

Zhao, P., and L. Chen, 2001: Interannual variability of atmospheric heat source/sink over the Qinghai—Xizang (Tibetan) Plateau and its relation to circulation. *Adv. Atmos. Sci.*, 18, 106-116.

Zhou, T., R. Yu, H. Chen, A. Dai, and Y. Pan, 2008: Summer Precipitation Frequency, Intensity, and Diurnal Cycle over China: A Comparison of Satellite Data with Rain Gauge Observations. *J. Climate*, 21, 3997-4010.

621 **Table Captions**

622 Table 1. Classification of the rainfall events based on the domain-averaged precipitation intensity
623 (PI).

624

625 **Figure Captions**

626 Fig. 1. Topography (m) of the domain and the selected regions: PRD, MLYR, and ETP, marked
627 with boxes.

628 Fig. 2. Daily precipitation (mm d^{-1}) from the TRMM (green) dataset, ERAINT (blue) and
629 simulations (pink) for the PRD (a), MLYR (b) and ETP (c). Letters r1 and r2 in the legend are
630 the correlation coefficients between the CRM and the TRMM, and the ERAINT respectively.

631 Fig. 3 Monthly averaged total cloud water content (g kg^{-1}) and temperature (°C) for the PRD (a,
632 b), MLYR (c, d) and ETP (e, f).

633 Fig. 4 Monthly averaged liquid water content and ice water content (g kg^{-1}) for the PRD (a, b),
634 MLYR (c, d) and ETP (e, f).

635 Fig. 5. Seasonal frequency of cloud base and cloud height all cloud cells for the PRD, MLYR
636 and ETP of the year 2010.

637 Fig. 6. Diurnal cycle of seasonal frequency of different precipitation intensities (mm hr-1) for
638 the PRD (a-d), the MLYR (e-h) and the ETP (i-l).

639 Fig. 7. Diurnal cycle of seasonal averaged frequency (%) of deep convections for the PRD (a-d),
640 the MLYR (e-h) and the ETP (i-l). Note that there is no deep convective cloud cell was
641 filtered out during winter for the ETP.

642 Fig. 8. Diurnal cycle of seasonal averaged total cloud water content (g kg-1) of deep convections
643 for the PRD (a-d), the MLYR (e-h) and the ETP (i-l). Note that there is no deep convective
644 cloud cell was filtered out during winter for the ETP.
645 Fig. 9. Diurnal cycle of seasonal averaged surface sensible heat flux (SH) and latent heat flux
646 (LH) over the ETP.
647 Fig. 10. Diurnal cycle of seasonal averaged total cloud water content (g kg-1) of shallow
648 cumulus for the PRD (a-d), the MLYR (e-h) and the ETP (i-l).
649 Fig. 11. Diurnal cycle of seasonal averaged frequency (%) of cumulus for the PRD (a-d), the
650 MLYR (e-h) and the ETP (i-l).
651
652

Table 1. Classification of the rainfall events based on the domain-averaged precipitation intensity (PI).

Type	**I**	**II**	**II**	**IV**	**V**
PI (mm hr^{-1})	PI ≤0.2	0.2 <PI ≤1	1 <PI ≤2.5	2.5 <PI ≤5	PI>5

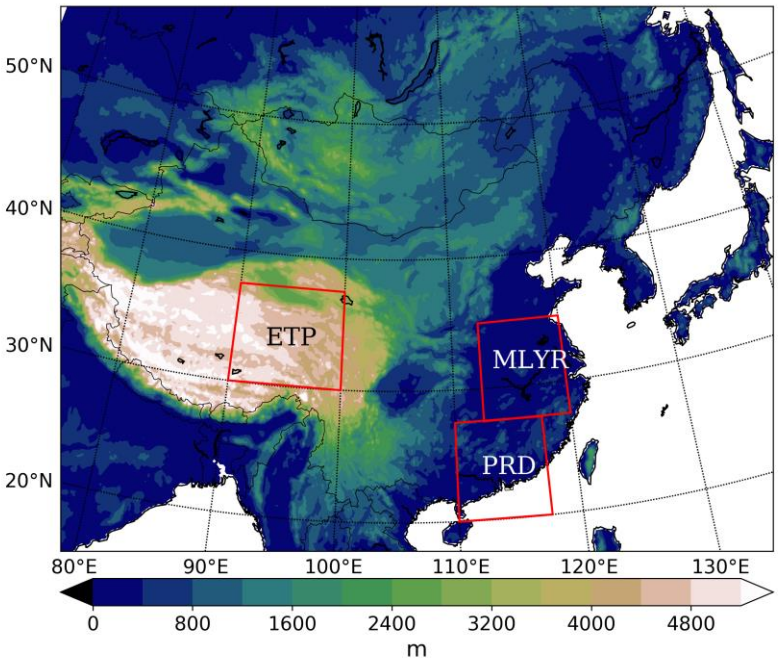

659

660 Fig. 1. Topography (m) of the domain and the selected regions: PRD, MLYR, and ETP, marked

661 with boxes.

662

663

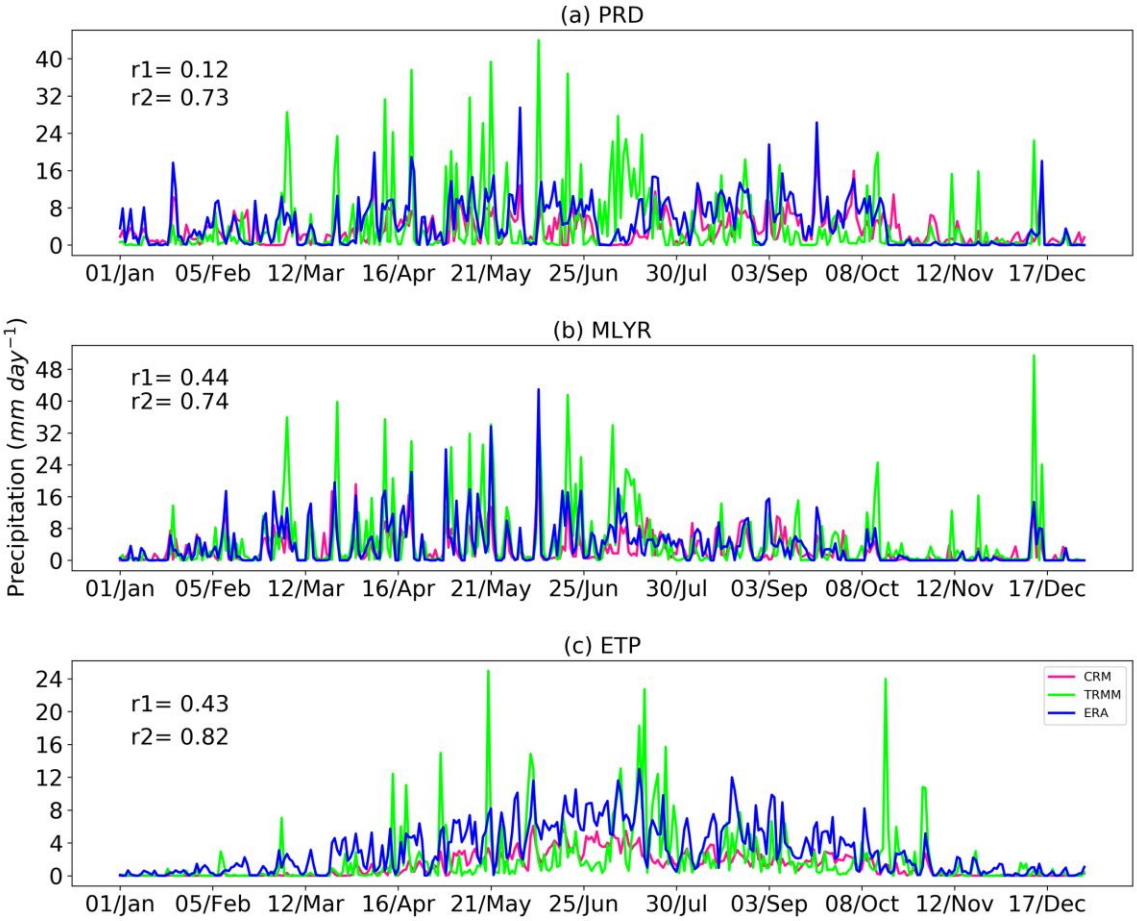

664

665 Fig. 2. Daily precipitation (mm d^{-1}) from the TRMM (green) dataset, ERAINT (blue) and

666 simulations (pink) for the PRD (a), MLYR (b) and ETP (c). Letters r1 and r2 in the legend are

667 the correlation coefficients between the CRM and the TRMM, and the ERAINT respectively.

668

669

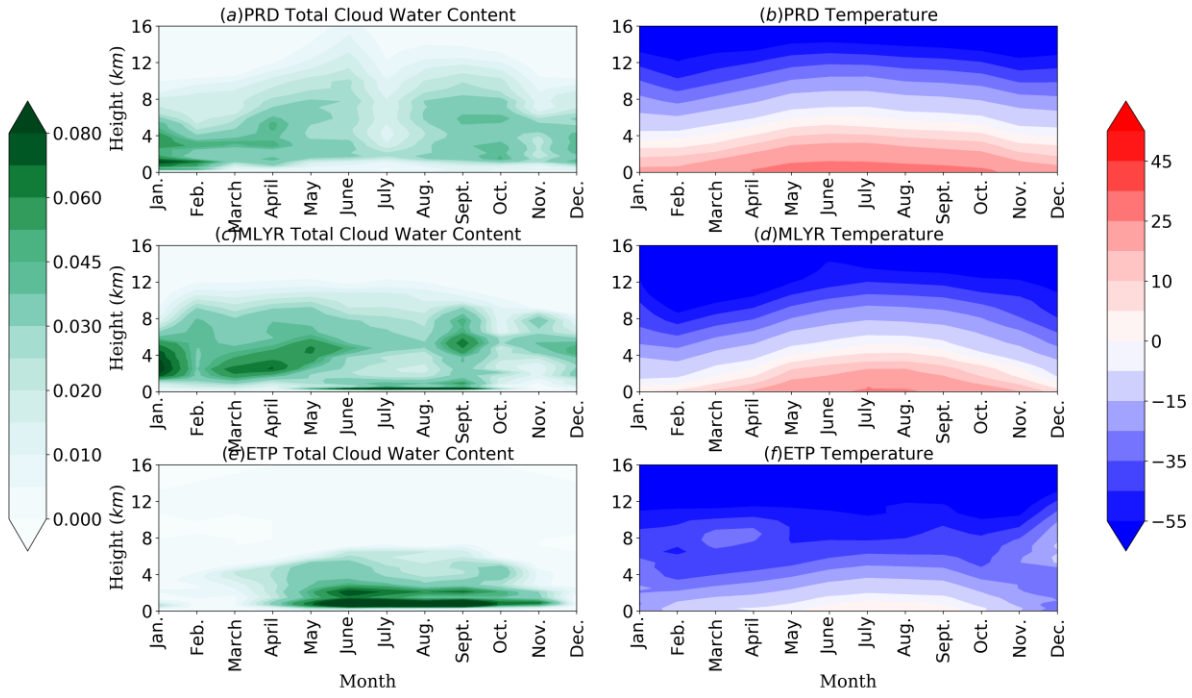

670

671 Fig. 3 Monthly averaged total cloud water content (g kg^{-1}) and temperature (°C) for the PRD (a,

672 b), MLYR (c, d) and ETP (e, f).

673

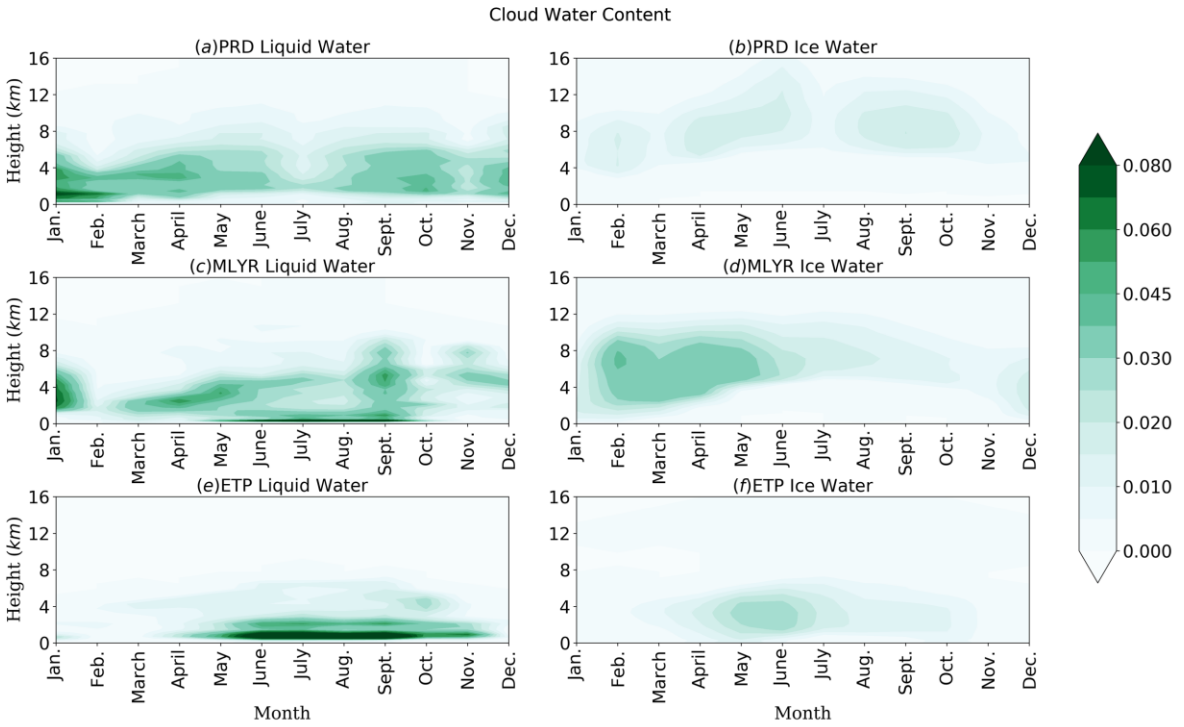

Fig. 4 Monthly averaged liquid water content and ice water content (g kg^{-1}) for the PRD (a, b), MLYR (c, d) and ETP (e, f).

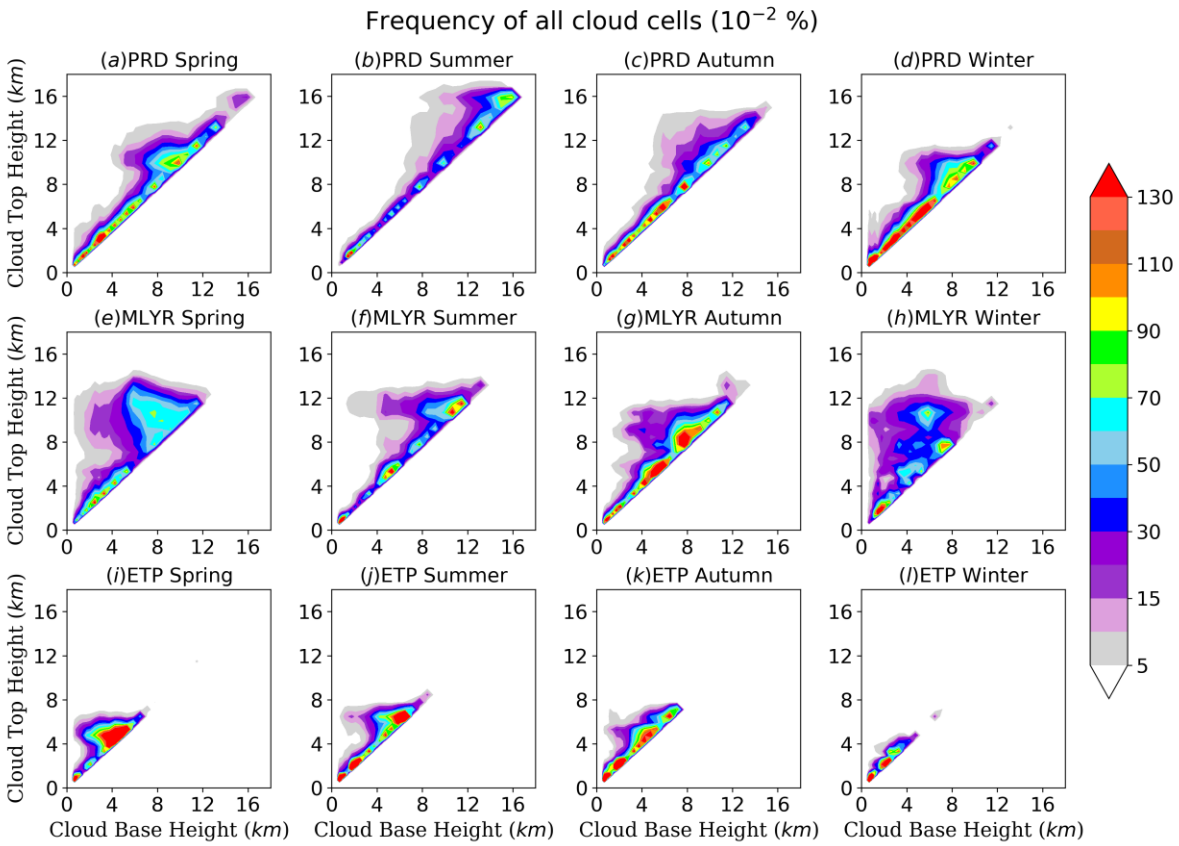

679

680 Fig. 5. Seasonal frequency of cloud base and cloud height all cloud cells for the PRD, MLYR

681 and ETP of the year 2010.

682

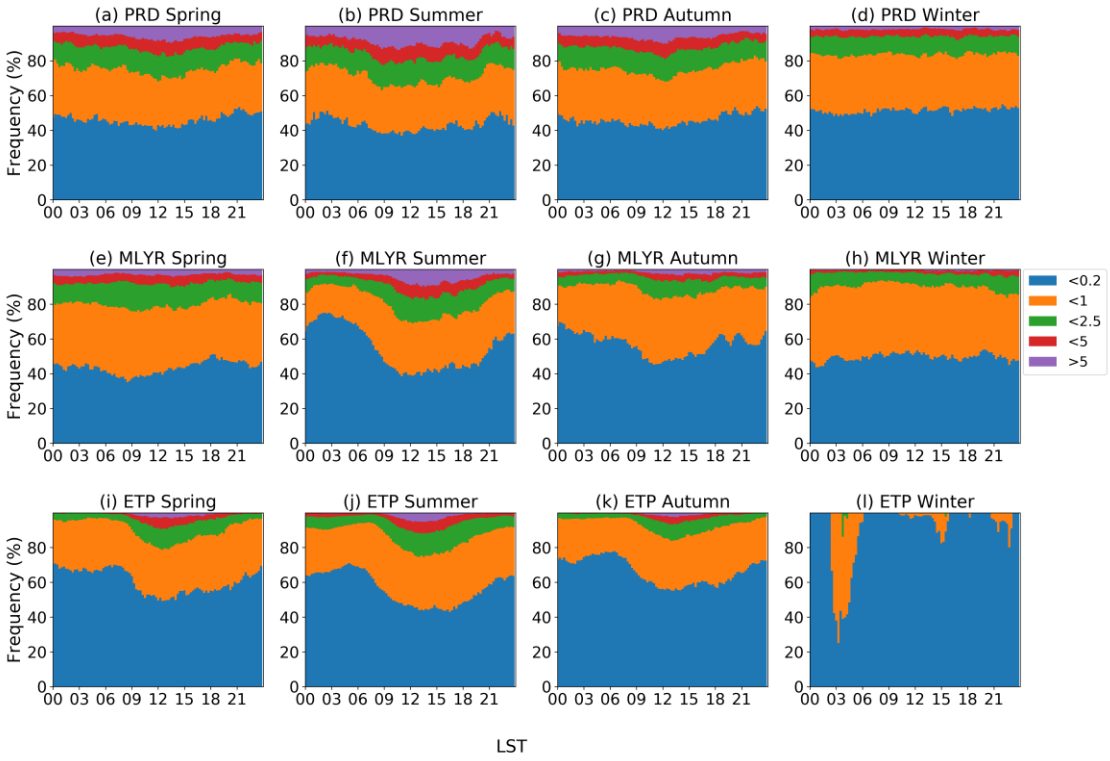

683

684 Fig. 6. Diurnal cycle of seasonal frequency of different precipitation intensities (mm hr-1) for

685 the PRD (a-d), the MLYR (e-h) and the ETP (i-l).

686

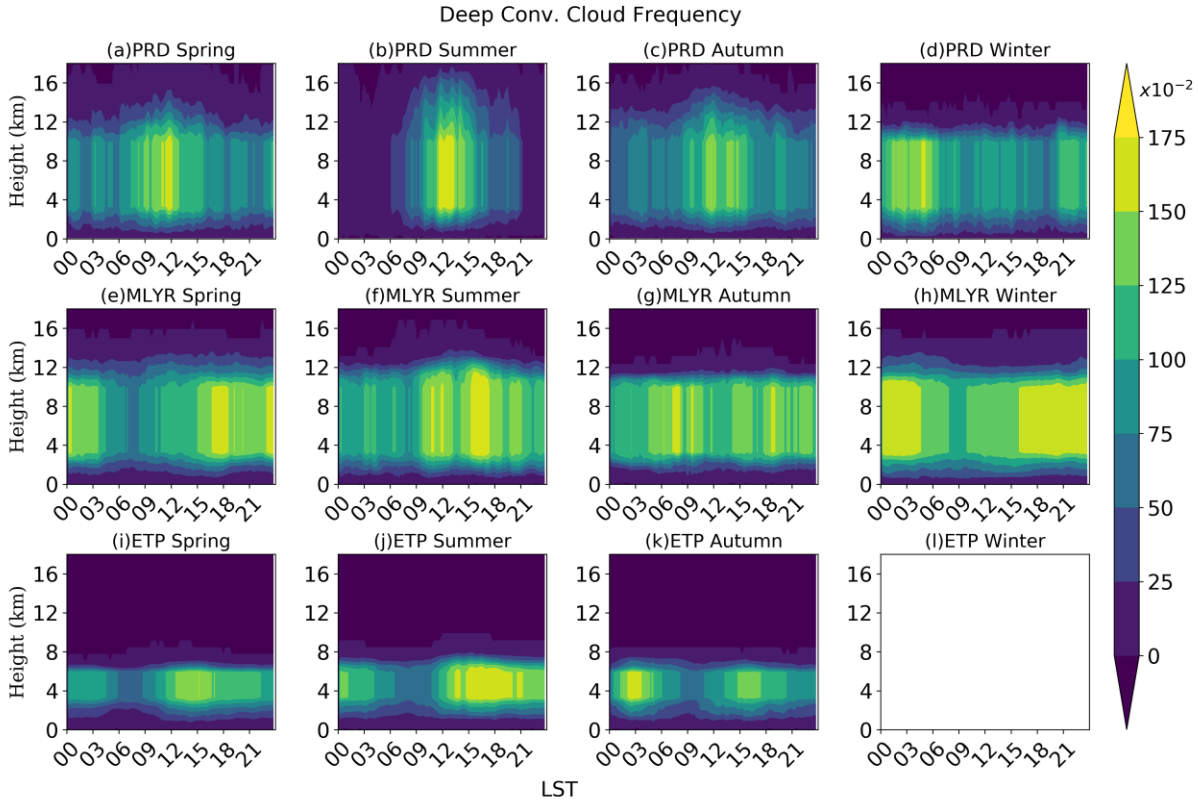

687

688 Fig. 7. Diurnal cycle of seasonal averaged frequency (%) of deep convections for the PRD (a-d),

689 the MLYR (e-h) and the ETP (i-l). Note that there is no deep convective cloud cell was filtered

690 out during winter for the ETP.

691

692

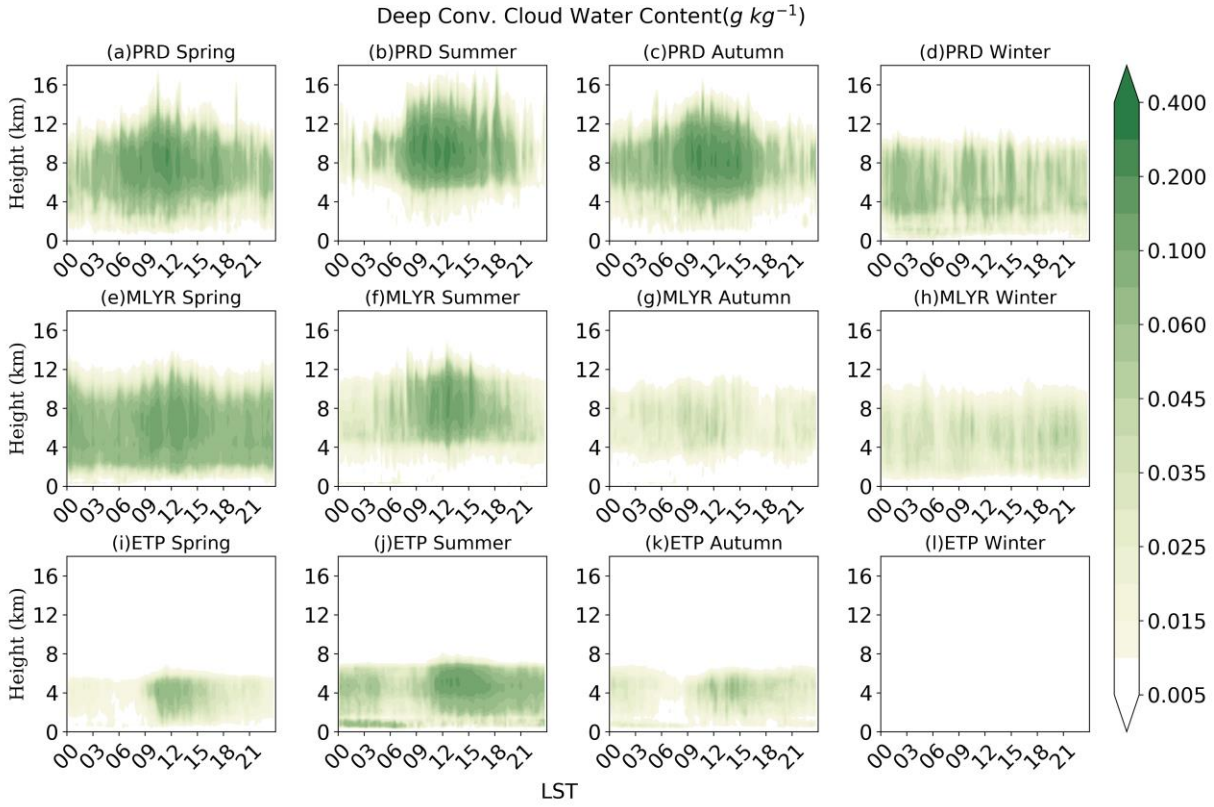

693

694 Fig. 8. Diurnal cycle of seasonal averaged total cloud water content (g kg-1) of deep convections

695 for the PRD (a-d), the MLYR (e-h) and the ETP (i-l). Note that there is no deep convective cloud

696 cell was filtered out during winter for the ETP.

697

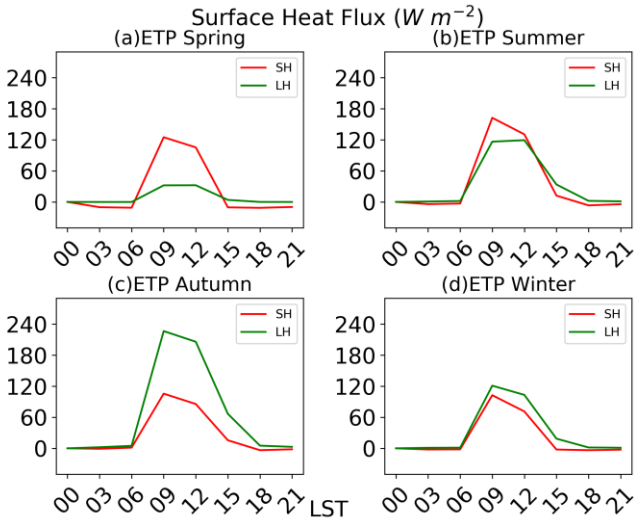

698

699 Fig. 9. Diurnal cycle of seasonal averaged surface sensible heat flux (SH) and latent heat flux

700 (LH) over the ETP.

701

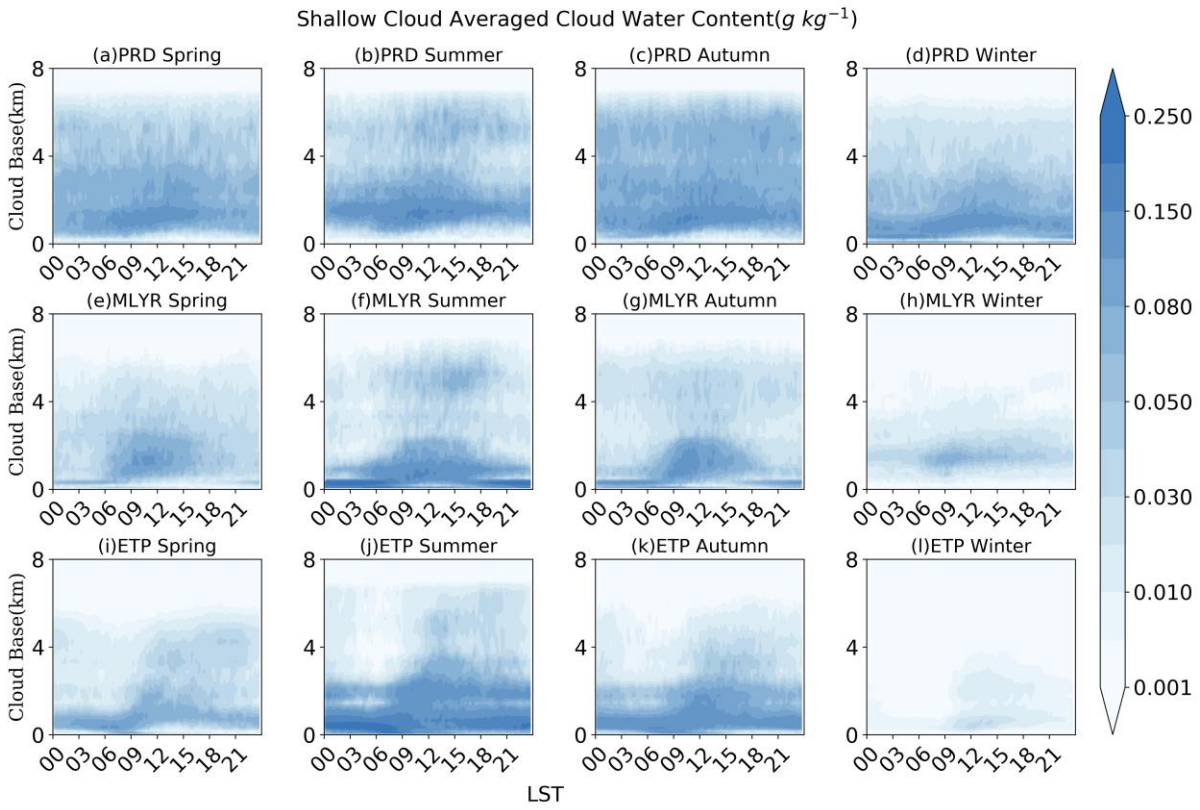

Fig. 10. Diurnal cycle of seasonal averaged total cloud water content (g kg-1) of shallow cumulus for the PRD (a-d), the MLYR (e-h) and the ETP (i-l).

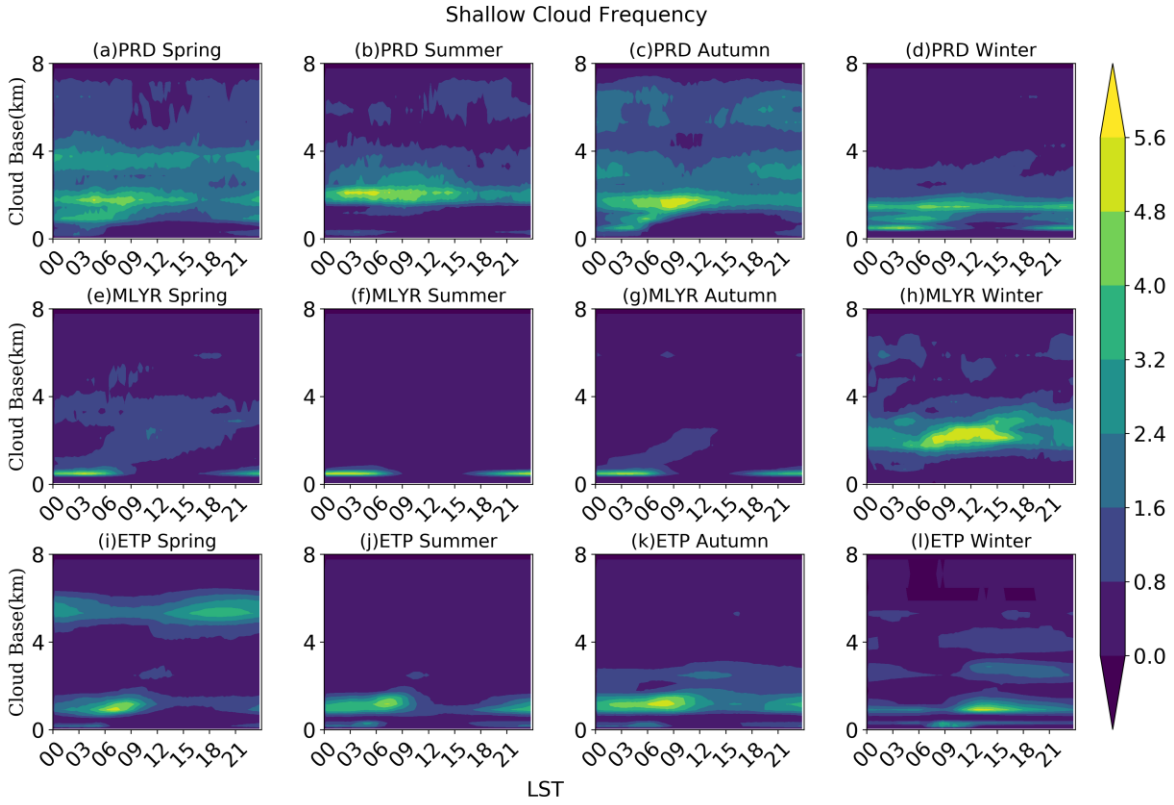

706

707 Fig. 11. Diurnal cycle of seasonal averaged frequency (%) of cumulus for the PRD (a-d), the

708 MLYR (e-h) and the ETP (i-l).

709

Figure1.

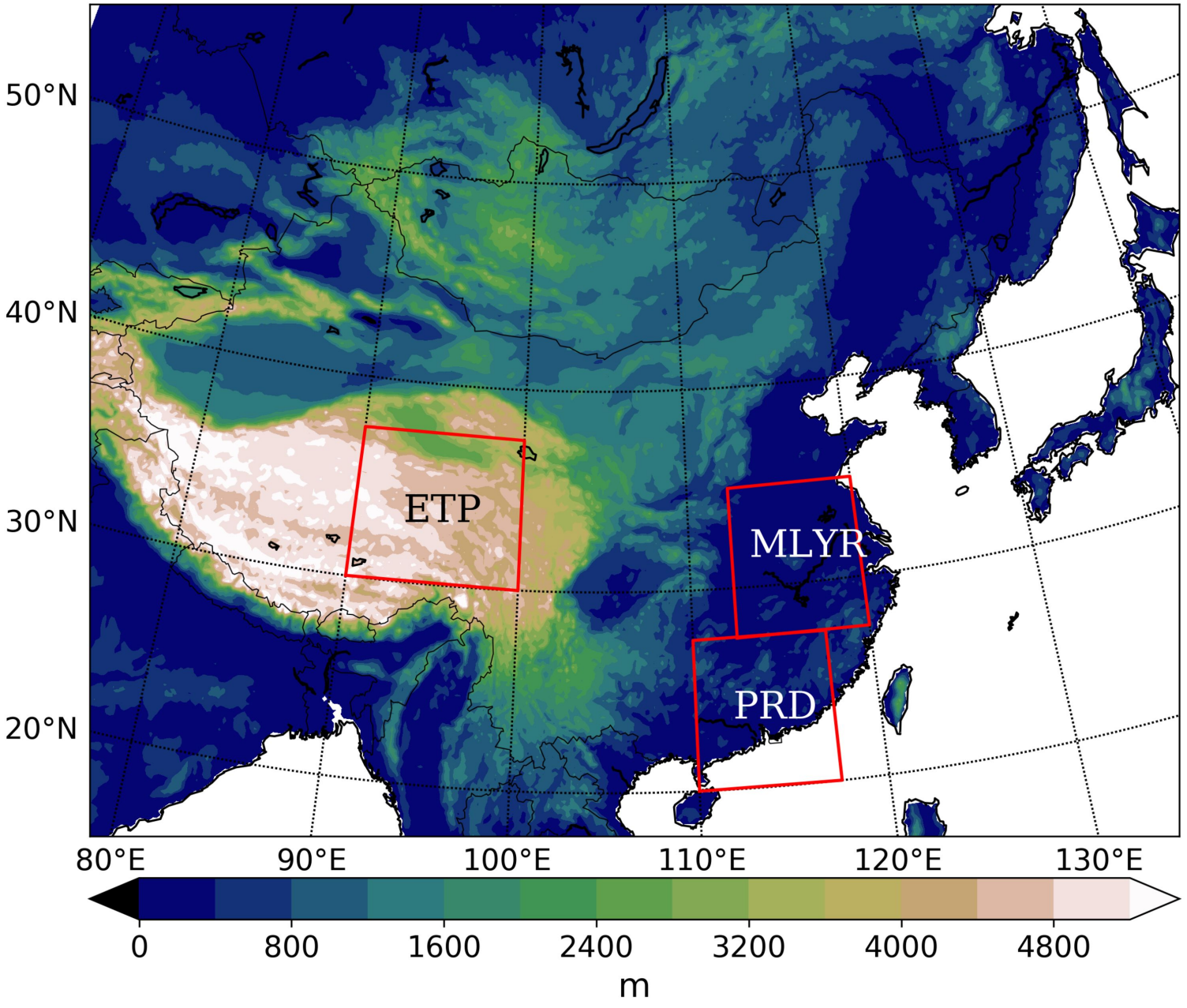
50°N
40°N
30°N
20°N
80°E
90°E
100°E
110°E
120°E
130°E
ETP
MLYR
PRD
0
800
1600
2400
3200
4000
4800
m

Figure2.

(a) PRD

r1= 0.12
r2= 0.73

40
32
24
16
8
0

01/Jan 05/Feb 12/Mar 16/Apr 21/May 25/Jun 30/Jul 03/Sep 08/Oct 12/Nov 17/Dec

(b) MLYR

Precipitation (*mm day*$^{-1}$)

r1= 0.44
r2= 0.74

48
40
32
24
16
8
0

01/Jan 05/Feb 12/Mar 16/Apr 21/May 25/Jun 30/Jul 03/Sep 08/Oct 12/Nov 17/Dec

(c) ETP

r1= 0.43
r2= 0.82

24
20
16
12
8
4
0

CRM
TRMM
ERA

01/Jan 05/Feb 12/Mar 16/Apr 21/May 25/Jun 30/Jul 03/Sep 08/Oct 12/Nov 17/Dec

Figure3.

(*a*)PRD Total Cloud Water Content

(*b*)PRD Temperature

(*c*)MLYR Total Cloud Water Content

(*d*)MLYR Temperature

(*e*)ETP Total Cloud Water Content

(*f*)ETP Temperature

Height (*km*)

16
12
8
4
0

Jan. Feb. March April May June July Aug. Sept. Oct. Nov. Dec.

Month

0.080
0.060
0.045
0.030
0.020
0.010
0.000

45
25
10
0
−15
−35
−55

Figure4.

Cloud Water Content

(*a*)PRD Liquid Water

(*b*)PRD Ice Water

(*c*)MLYR Liquid Water

(*d*)MLYR Ice Water

(*e*)ETP Liquid Water

(*f*)ETP Ice Water

Height (*km*)

0 4 8 12 16

Jan. Feb. March April May June July Aug. Sept. Oct. Nov. Dec.

Month

0.080 0.060 0.045 0.030 0.020 0.010 0.000

Figure5.

Frequency of all cloud cells (10^{-2} %)

(*a*)PRD Spring | (*b*)PRD Summer | (*c*)PRD Autumn | (*d*)PRD Winter

(*e*)MLYR Spring | (*f*)MLYR Summer | (*g*)MLYR Autumn | (*h*)MLYR Winter

(*i*)ETP Spring | (*j*)ETP Summer | (*k*)ETP Autumn | (*l*)ETP Winter

Cloud Top Height (*km*)

Cloud Base Height (*km*)

0 4 8 12 16

130 110 90 70 50 30 15 5

Figure6.

(a) PRD Spring
(b) PRD Summer
(c) PRD Autumn
(d) PRD Winter
(e) MLYR Spring
(f) MLYR Summer
(g) MLYR Autumn
(h) MLYR Winter
(i) ETP Spring
(j) ETP Summer
(k) ETP Autumn
(l) ETP Winter
Frequency (%)
0
20
40
60
80
00 03 06 09 12 15 18 21
LST
<0.2
<1
<2.5
<5
>5

Figure7.

Deep Conv. Cloud Frequency

(a)PRD Spring
(b)PRD Summer
(c)PRD Autumn
(d)PRD Winter
(e)MLYR Spring
(f)MLYR Summer
(g)MLYR Autumn
(h)MLYR Winter
(i)ETP Spring
(j)ETP Summer
(k)ETP Autumn
(l)ETP Winter

Height (km)
0
4
8
12
16
00 03 06 09 12 15 18 21
LST

$x10^{-2}$
140
120
100
80
60
40
20
0

Figure8.

Deep Conv. Cloud Water Content($g\ kg^{-1}$)

(a)PRD Spring | (b)PRD Summer | (c)PRD Autumn | (d)PRD Winter

(e)MLYR Spring | (f)MLYR Summer | (g)MLYR Autumn | (h)MLYR Winter

(i)ETP Spring | (j)ETP Summer | (k)ETP Autumn | (l)ETP Winter

Height (km)

0 4 8 12 16

00 03 06 09 12 15 18 21

LST

0.400 0.200 0.100 0.060 0.045 0.035 0.025 0.015 0.005

Figure9.

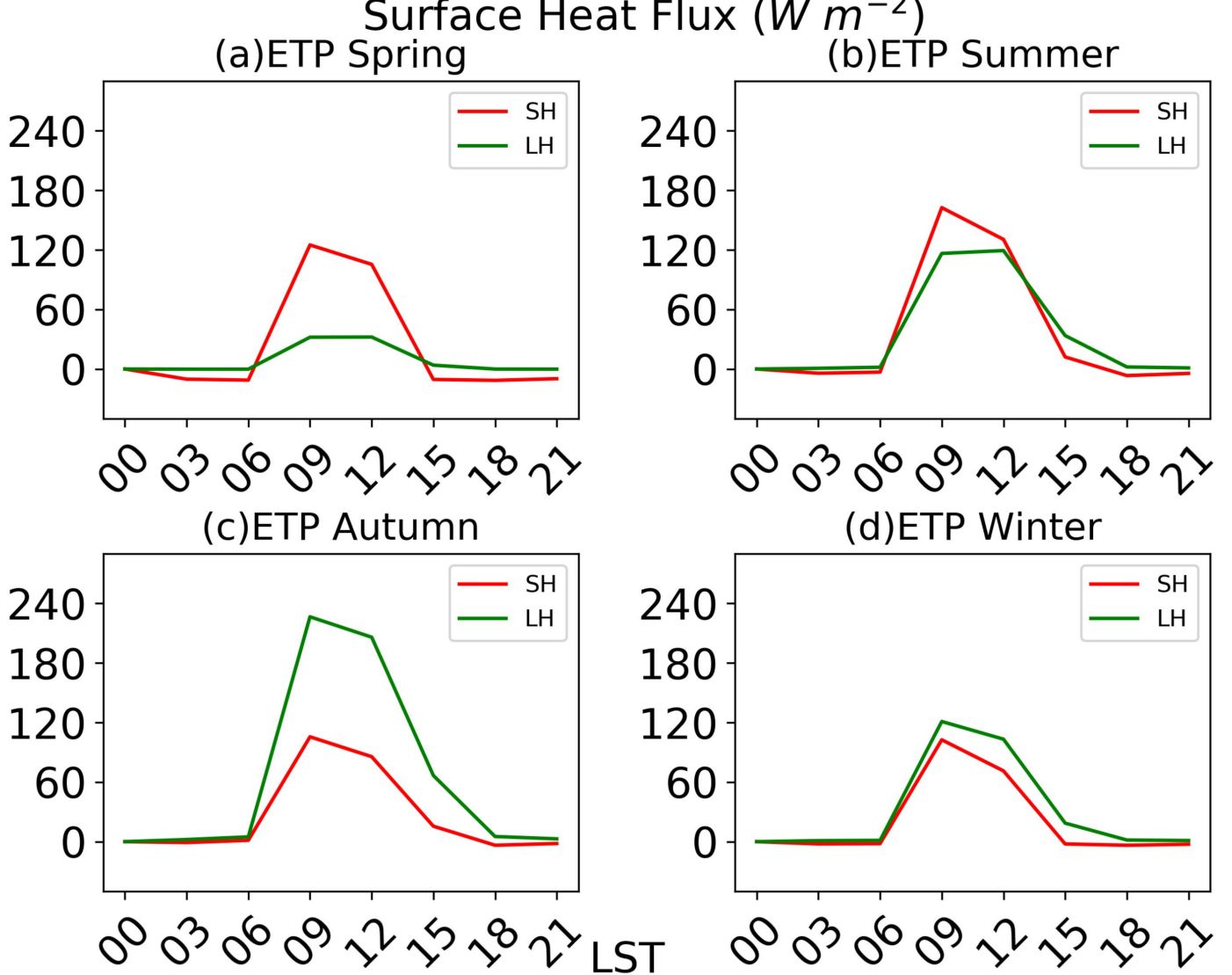
Surface Heat Flux ($W\ m^{-2}$)
(a)ETP Spring
(b)ETP Summer
(c)ETP Autumn
(d)ETP Winter
SH
LH
240
180
120
60
0
00
03
06
09
12
15
18
21
LST

Figure10.

Cumulus Averaged Cloud Water Content($g\ kg^{-1}$)

(a)PRD Spring
(b)PRD Summer
(c)PRD Autumn
(d)PRD Winter
(e)MLYR Spring
(f)MLYR Summer
(g)MLYR Autumn
(h)MLYR Winter
(i)ETP Spring
(j)ETP Summer
(k)ETP Autumn
(l)ETP Winter

Cloud Base(km)
0
4
8
00 03 06 09 12 15 18 21
LST

0.250
0.150
0.080
0.050
0.030
0.010
0.001

Figure11.

Cumulus Frequency

(a)PRD Spring
(b)PRD Summer
(c)PRD Autumn
(d)PRD Winter
(e)MLYR Spring
(f)MLYR Summer
(g)MLYR Autumn
(h)MLYR Winter
(i)ETP Spring
(j)ETP Summer
(k)ETP Autumn
(l)ETP Winter

Cloud Base(km)

0
4
8

00 03 06 09 12 15 18 21

LST

5.6
4.8
4.0
3.2
2.4
1.6
0.8
0.0